1   Modeling stem cell nucleus mechanics using confocal microscopy

2

3   Kennedy Z[1], Newberg J[1], Goelzer M[1], Stefan Judex[2], Fitzpatrick CK[1], Uzer G[1] [†]

4   [1]Mechanical and Biomedical Engineering, Boise State University

5   [2]Biomedical Engineering, Stony Brook University

6

7   [†] **Corresponding Author:**

8   Gunes Uzer PhD

9   Boise State University

10   Department of Mechanical and Biomedical Engineering

11   1910 University Drive, MS-2085

12   Boise, ID 83725-2085

13   Ph. (208) 426-4461

14   **Email: gunesuzer@boisestate.edu**

15

18

19   **Authors' contributions**

20   **Kennedy Z** data analysis/interpretation, manuscript writing, final approval of manuscript.

21   **Newberg J** data analysis/interpretation, data analysis.

22   **Goelzer M** data analysis/interpretation, data analysis, final approval of manuscript.

23   **Judex S** data analysis/interpretation, manuscript writing, final approval of manuscript

24   **Fitzpatrick CK** financial support, data analysis/interpretation, final approval of manuscript

25   **Uzer G** concept/design, financial support, data analysis/interpretation, manuscript writing, final

26   approval of manuscript

27

Conflicts of interest/Competing interests

The author(s) declare no competing interests financial or otherwise.

30

Ethics approval

All methods were carried out in accordance with relevant guidelines and regulations of Boise

Institutional Animal Care and Use Committee and Institutional Biosafety Committee. All

procedures were approved by Boise State University Institutional Animal Care and Use

Committee, and Institutional Biosafety Committee.

36

Consent for publication

All authors consent to publication

39

Availability of data and material

The datasets generated and/or analyzed during the current study are available from the

corresponding author on reasonable request.

43

Code availability

The code generated and/or analyzed during the current study are available from the

corresponding author on reasonable request.

47

Abstract

Nuclear mechanics is emerging as a key component of stem cell function and differentiation.

While changes in nuclear structure can be visually imaged with confocal microscopy,

mechanical characterization of the nucleus and its sub-cellular components require specialized

testing equipment. A computational model permitting cell-specific mechanical information

53   directly from confocal and atomic force microscopy of cell nuclei would be of great value. Here,

54   we developed a computational framework for generating finite element models of isolated cell

55   nuclei from multiple confocal microscopy scans and simple atomic force microscopy (AFM)

56   tests. Confocal imaging stacks of isolated mesenchymal stem cells (MSC) were converted into

57   finite element models and siRNA-mediated LaminA/C depletion isolated chromatin and

58   LaminA/C structures. Using AFM-measured experimental stiffness values, a set of conversion

59   factors were determined for both chromatin and LaminA/C to map the voxel intensity of the

60   original images to the element stiffness, allowing the prediction of nuclear stiffness in an

61   additional set of other nuclei. The developed computational framework will identify the

62   contribution of a multitude of sub-nuclear structures and predict global nuclear stiffness of

63   multiple nuclei based on simple nuclear isolation protocols, confocal images and AFM tests.

64

65   **Key words:** Finite Element Analysis, Mesenchymal Stem Cells, Nucleus, Mechanobiology,

66   LaminA/C, Chromatin, Confocal Microscopy

67

68   **Introduction**

69   All living organisms function in and adapt to mechanically active environments at the levels of

70   the organ, tissue, and cell. Mesenchymal stem cells (MSC) are the tissue resident stem cells of

71   musculoskeletal tissues that, at least in part, regulate the adaptive response to mechanical

72   challenge by proliferating and differentiating into distinct cell types[1]. MSC stem cell

73   differentiation is heavily influenced by the stiffness of the extracellular matrix[2]. For instance,

74   plating MSCs onto soft or stiff substrates can drive MSC differentiation towards adipogenesis or

75   osteogenesis, respectively[3]. The means by which MSC can sense the stiffness of its

76   extracellular matrix comprise an interplay of focal adhesions, the cytoskeleton, and the nucleus[4].

77   When a MSC is placed onto a stiffer extracellular matrix, the cell will increase its size and the

78   number of focal adhesions to its extracellular matrix[5], promoting cell traction within the

79 extracellular matrix[4]. As the cell spreads on the extracellular matrix, actin microfilaments tug on

80 the nucleus causing it to stretch and deform[6]. These changes in the nuclear structure are critical

81 for cell function. For example, the nuclear membrane is covered with nuclear pore complexes

82 that are sensitive to cytoskeletal deformations of the nucleus[7]. When these pores are opened,

83 the transcriptional factors such as YAP/TAZ are allowed into the nucleus to regulate gene

84 expression[8]. Further, chromatin itself is responsive to mechanical challenge, as the application

85 of mechanical forces can alter heterochromatin dynamics and organization[9,10]. While signaling

86 events such as YAP/TAZ and DNA changes are areas of active research, probing nuclear

87 mechanical properties in living cells remain challenging.

88

89 Quantifying the bulk mechanical properties of the nucleus can be performed via atomic force

90 microscopes, micropipette setups, optical tweezers, or microfluidics[11]. While single-cell level

91 optical methods to measure intra-nuclear deformations are emerging[12], cellular FE models that

92 can capture nuclear structure and predict nuclear mechanics of many nuclei could provide

93 mechanistic information on cell's mechanical properties and at the same time, present a time-

94 saving and cost-effective alternative. The stiffness of the nucleus is primarily affected by two

95 nuclear components, LaminA/C and chromatin[13]. LaminA/C is a protein that scaffolds the inner

96 nuclear membrane, adding mechanical stiffness to the nucleus while Lamin B does not

97 contribute to nuclear mechanics[14]. Chromatin is made of compact DNA and histones that

98 occupies the interior of the nucleus and also provides mechanical competence[15,16]. Thus,

99 inclusion of these two components is essential for modeling nuclear mechanics.

100

101 Here, we propose and validate a method that uses imaging intensity data from confocal images

102 from LaminA/C and chromatin to determine nuclear mechanical properties. To this end, we

103 developed a computational framework capable of producing confocal-image-based finite

104 element models of an MSC nucleus that replicates the structural configuration of both chromatin

105 and LaminA/C. Finite element models constructed with image intensity based elasticity values

106 were calibrated using experimental AFM measurements of cell nuclei with or without LaminA/C.

107 This model was then tested in its ability to predict the stiffness of two additional test nuclei.

108

Data Collection, Modeling, Simulation Setup and Methods

110 Cell Culture

111 MSCs were harvested from the bone marrow of 8-wk old male C57BL/6J mice as previously

112 described.[17,18] Cells used for the experiments were between passage 7 and passage 11. Cells

113 were sub-cultured at a density of 1,800 cells/cm^2 and maintained within IMDM (12440053,

114 GIBGO) with 10% FCS (S11950H, Atlanta Biologicals) with 1% Pen/strep (GIBCO).

115

116 Nucleus Isolation

117 MSCs were scraped off their plates using 9 mL of 1x PBS and centrifuged at 1100 RPM at 4°C

118 with a Beckman Coulter Allegra X-30R Centrifuge. MSCs were suspended within 500 μL

119 hypotonic buffer A (.33M Sucrose, 10mM HEPES, pH 7.4, 1mM MgC12, 0.5% w/v Saponin) and

120 centrifuged twice at 3000 RPM, 4°C for 10 minutes using a Beckman Coulter Microfuge 20R

121 Centrifuge. Cytoplasmic supernatant was aspirated away and the remaining nuclei were

122 resuspended using 100 μL of hypotonic buffer A. Cytoplasmic debris was separated from the

123 nuclei by adding 400 μL of Percoll. The resulting mixture was centrifuged at 10,000 RPM at 4°C

124 for 10 minutes. Nuclei were then plated in a .01 Poly-L-Lysine coated 35 mm cell culture dish

125 and incubated for 25 minutes.

126

127 Nucleus Stiffness Data Using AFM

128 Force-displacement curves of isolated nuclei were acquired using a Bruker Dimension FastScan

129 Bio AFM. Tipless MLCT-D probes (0.03 N/m spring constant) were functionalized with 10 μm

130 diameter borosilicate glass beads (Thermo Scientific 9010, 10.0 ± 1.0 μm NIST-traceable 9000

131   Series Glass Particle Standards) prior to AFM experiments using UV-curable Norland Optical

132   Adhesive 61 and, a thermal tune was conducted on each probe immediately prior to use to

133   determine its spring constant and deflection sensitivity. Nuclei were located using the AFM's

134   optical microscope and engaged with a 2-3nN force setpoint to ensure contact prior to testing.

135   After engaging on a selected nucleus, force curve ramping was performed at a rate of 2 µm/sec

136   over 2 µm total travel (1 µm approach, 1 µm retract). Three replicate force-displacement curves

137   were acquired and saved for each nucleus tested, with at least 3 seconds of rest between

138   conducting each test. Measurements that showed less than 600 nm contact with the nucleus

139   were discarded. Measured force-displacement curves were than exported into Matlab

140   (Mathworks, Natick, MA) to generate a curve of points that reflects the mean of the force to

141   displacement curve as well as the standard deviation of the atomic force microscopy

142   experiments.

143

144   Nucleus Imaging

145   A singe group of MSC was grown within control conditions and isolated using the methods

146   described above. The chromatin of the nuclei was then stained with Hoechst 33342 while the

147   LaminA/C was stained with mAB 4777 (Abcam). 5 nuclei were then imaged using a Nikon A1

148   confocal microscope at a rate of .2 µm out of plane and .05 µm in plane resolution.

149

150   *Measuring Stiffness of Intact and LaminA/C Depleted Cell Nuclei*

151   As we sought to model nuclear stiffness based on confocal images of LaminA/C and chromatin,

152   we first obtained mechanical properties of cell nuclei isolated from live MSCs with or without

153   LaminA/C. Two groups of MSCs were cultured in growth media (IMDM, 10% fetal bovine serum,

154   1%Pen Strep). One group received a LaminA/C specific siRNA treatment (siLamin), ceasing

155   LaminA/C mRNA expression in MSCs while the other group was treated with a non-specific

156   control siRNA (siControl). 48h after siRNA treatment, cell nuclei were isolated, plated onto 0.1%

157   Poly-L-Lysine coated plates for adherence and subjected to AFM testing to obtain force-

158   displacement curves as we reported previously (**Fig. 1a**)[19]. As shown in immunolabeled nuclei

159   images (**Fig. 1b**), isolated control nuclei appeared round and maintained intact LaminA/C (red)

160   and DNA (blue) confirmation. Shown in **Fig.1c**, force-displacement curves for siControl (N=30)

161   and siLamin (N=73) groups were obtained by shows that the maximum force measured at the

162   AFM tip for the siLamin group was, on average, 59% smaller than the siControl group (p<0.05,

163   Fig. 1c), confirming that nuclei are softer without LaminA/C[14].

164

165   <u>Mesh Generation from Confocal Scans</u>

166   To model the contribution of LaminA/C and chromatin separately, we generated two volumetric

167   meshes from each nucleus image. The first mesh was generated using the chromatin signal of

168   the nucleus image and the second one was generated using the LaminA/C signal of the nucleus

169   image. For chromatin, the 3D confocal image of the chromatin was imported into Amira software

170   (ThermoFisher, MA) and the nucleus geometry was manually segmented (**Fig. 2a**). A surface

171   mesh was created that employed triangular S3 elements surrounding the nucleus geometry

172   (**Fig. 2b**). This surface mesh was then imported into Hypermesh (Altair Engineering, MI) to

173   create a volume mesh with C3D4 tetrahedral elements (**Fig. 2c**). The resulting volume mesh

174   was imported into Bonemat software (http://www.bonemat.org/) (**Fig. 2d)** to overlay the

175   volumetric mesh onto the original confocal image and to assign stiffness values to each

176   tetrahedral element using the average voxel intensity (HU) within each element (Equation 1):

177   $$E = a + b * HU^c \qquad\qquad \text{(Equation 1)}$$

178   The term **a,** representing the intensity-independent elastic modulus, was set to "0" to eliminate

179   any contribution to elasticity outside the image intensity. Terms **b** and **c** are a set of conversion

180   factors defined during each experiment. Here, we used a linear isotropic elastic material

181   definition with a Poisson's ratio of 0.5 for each model[20]. For this study, FE meshes were

182   generated for five isolated nuclei. Two representations of each nucleus were generated; one

183   that included both LaminA/C and chromatin, and one which included only chromatin. All the

184   nuclei were imaged via a Nikon A1 confocal microscope with an image depth of .2 μm and a

185   voxel width of .05 μm.

186

187   To generate a model that contains both LaminA/C and chromatin (i.e. LaminA/C + chromatin

188   mesh), two identical nucleus geometries were produced. Chromatin meshes were assigned

189   elasticity values using the siLamin nuclei force-displacement curves (i.e. no LaminA/C present).

190   While siRNA procedure does not deplete the entire LaminA/C protein levels, a large decrease in

191   measured force value (**Fig.1c**) shows a substantial decline. The effectiveness of this siRNA

192   procedure was confirmed in a recent publication[21]. Conversion factors for the LaminA/C meshes

193   were derived via utilizing the chromatin mesh elasticity values and the the AFM data for intact

194   nuclei (i.e. siControl nuclei with both Lamin A/C and chromatin present). The chromatin and

195   LaminA/C elasticities in each element were then linearly added to produce the siControl model

196   containing the elasticity of both structures.

197

198   <u>Replicating AFM Experiments *in silico*</u>

199   Atomic force microscopy simulations were performed in ABAQUS software (2019, Dassault

200   Systemes, France). A replica of the AFM test setup was modeled *in silico* (**Fig. 2e**). The bottom

201   node layer of the nucleus model (red) was fixed to a rigid plane in all orthogonal directions to

202   simulate the nucleus being attached to the poly-L-Lysine coated plate surface. A simulated AFM

203   tip (yellow) was created by positioning a sphere (r=5 μm) made of C3D4 elements with a rigid

204   body material definition above the nucleus model. Contact between the nucleus and the AFM tip

205   was defined as a no-friction contact pair. During simulation, the AFM tip was lowered onto the

206   nucleus until 1 μm indentation was reached (**Fig. 2f**). The required force to indent the nucleus

207   was recorded. The recorded force-displacement curves were used to quantify the root mean

208   squared error (RMSE) between experimental and *in silico* conditions.

209

210   Determination of the Element Volume for Nucleus Models

211   To determine the dependence of the AFM indentation force on the volume of the mesh

212   elements, nucleus models were constructed from 5 chromatin nuclei images with element

213   volumes of 5, 4, 3, 2, 1, .8, and .6 μm^3. The models were assigned temporary elasticity values

214   using the original chromatin images with conversion factors of $a = 0$, $b = 20$, and $c = 1$. The

215   term a was set to 0 because of the assumption that there is no base elasticity independent of

216   image intensity, b was set to 20 and c was set to 1 to scale elasticity *linearly* to image voxel

217   intensity. A representative image for the meshes of nucleus#1, with varying element volumes

218   and with the original images at each mid-orthogonal plane is depicted in **Fig. 3a**. Each nucleus

219   model was subjected to *in silico* AFM experiments. For each nucleus model, the force

220   generated at 1 μm of indentation was recorded and plotted against element volume for each

221   nucleus **(Fig.3b)**. The mean maximum force value and standard deviation started to plateau for

222   element volumes of 1 μm^3 or smaller, indicating this volume that can be used without affecting

223   the maximum force output (green line).

224

225   Sensitivity of Image Noise to Element Volume

226   While force sensitivity analysis revealed a cut-off at 1 μm^3, we also sought to quantify how well

227   element volumes represented the spatial information from confocal images, as this may be

228   important for discerning nuclear deformation patterns. To accomplish this, we only used a

229   chromatin mesh without LaminA/C. Chromatin images for a single nucleus image (Nucleus #1)

230   was converted into six finite element models meshed with average element sizes of 3, 2, 1.5, 1,

231   .8, .6, and .3 μm^3 and assigned elasticity values using the temporary conversion factors $a = 0$, b

232    $= 20$, and $c = 1$. A Matlab script extracted a 3D image from each mesh with the 2D image from a

233   transverse plane (Z=7 μm) **(Fig. 4**, top row).

234

235   These images were then superimposed onto the original image (**Fig. 4**, second row) and the

236   intensity of each voxel was compared to each voxel in the original image, producing a color map

237   indicating the percent difference (**Fig. 4**, third row). Microscopy noise in the confocal images

238   was accounted for by comparing the average intensity of the DNA free region of interest to each

239   voxel within that region (**Fig. S2**). This analysis produced an average error value of 13%,

240   indicating the amount of inherent noise in the confocal images. This value was subtracted from

241   each voxel to quantify the non-noise related error. These corrected voxel errors were then

242   averaged to generate a final error value (**Fig.4**, bottom row). At 3 μm^3 element volume, the

243   average error was 12.3%. As element size decreased, the % error also decreased. At 1 μm^3,

244   the average error was 6.4%. For 1 μm^3 down to 0.3 μm^3, the average error only changed by

245   1.9% indicating a similar cut-off range where 1 μm^3 voxel volumes can represent 93.6% of the

246   chromatin configuration.

247

248   Response Surface Generation

249   To identify the sensitivity of the RMSE between experimental and *in silico* force-displacement

250   curves to different combinations of the b and c terms, two response surfaces were generated;

251   first, a coarse 8 X 8 matrix that was followed up by a finer 10 X 10 matrix. The c values were

252   spaced linearly while the *b* values were spaced logarithmically because of the much greater

253   change of b value, that minimized error, compared to the c value. To generate the RMSE

254   between experimental and *in silico* force-displacement curves, all five nuclei confocal

255   microscopy scans were converted to finite element models with an average element size of 1

256   μm^3. Each model was assigned elasticity values using the original image and the conversion

257   factors for the given datapoint. All five nucleus models then underwent a simulated atomic force

258   microscopy experiment where force-displacement data from the first 1 μm of nucleus

259   indentation was collected. The resulting force displacement curves were compared to the mean

260   atomic force microscopy curve taken from the experimental AFM indentations, calculating the

261   RMSE. The RMSE of all 5 models were averaged to create each point of the response surface.

262

263   Conversion Factor Optimization

264   Nucleus models #1, #2, and #3 were selected and converted to finite element models with an

265   element volume of 1 µm^3. The matlab algorithm "fmincon" was set to use an "SQP" optimization

266   algorithm with constraint/step tolerance set to 1x10^{-9} µN/µm^2. The c term was then constrained

267   to either $c = 1$ for linear material conversion or $c = 0$ for homogeneous material value. A value

268   of b = 1E-10 µN/µm^2 was used as a starting point. This algorithm optimized the b value until the

269   optimization constraint/step tolerance was met.

270

271   Statistical Analysis

272   Results were presented as mean ± one standard deviation (SD) unless indicated in figure

273   legends. For comparisons between groups, a non-parametric two-tailed Mann-Whitney U-test

274   was used. P-values of less than 0.05 were considered significant.

275

276   **Results**

277   Linear relationship between voxel intensity and material property is sufficient for assigning

278   material properties for both SiLamin and SiControl models

279   To determine the best set of conversion factors for creating nuclei models containing a

280   chromatin mesh only, an 8 X 8 response surface was generated to compare the simulated AFM

281   results to experimental AFM data for the LaminA/C depleted nuclei (**Fig. 5a)**. The b values were

282   logarithmically spaced between 1x10^{-9} µN/µm^2 and 1x10^{-3} µN/µm^2 and c values were linearly

283   spaced between 0.5 and 5. The error associated with each b-c combination was found by

284   generating the root mean squared error between the simulated and experimental AFM data.

285   Results showed that for every c value, there was a b value that minimized the error. To expand

286   on this finding, we selected the two *c* values of 0.5 and 1.1 that produced a minimum value

287   within our original 8 X 8 grid (green dotted boxes). Shown in **Fig.5b**, plotting a refined 10 X 10

288   response surface around these two *b-c* values, a minimum error along a straight line for

289   different *b* values was visible (dotted red lines), suggesting that minimizing the error was

290   independent of the initial *c* value. Shown in bottom right, setting *c*=1 produced a similar set of *b*

291   values that minimized the error between the simulated and the real AFM experiments, indicating

292   that a linear conversion between pixel intensity and modulus of elasticity could be used.

293

294   Repeating the same procedure using the LaminA/C + chromatin mesh and AFM data from intact

295   nuclei exhibited a similar outcome. We again found that the two *c* values of 0.5 and 1.1

296   produced a minimum value within our original 8 X 8 grid (green dotted boxes). For the first

297   minimum value, a 10 X 10 surface centered on $b = 3.7 \times 10^{-7}$ μN/μm^2 and $c = 1.1$ was generated.

298   For the second minimum, we created a surface centered on $b = 1.9 \times 10^{-5}$ μN/μm^2 and $c = 0.5$.

299   Both surfaces showed a minimum error along a straight line for different *b* values (dotted red

300   lines). Comparing these values to another 10 X 10 surface centered on $b = 1 \times 10^{-7}$ μN/μm^2 and

301     $c = 1$ showed a similar pattern, indicating that a linear relationship between voxel intensity and

302   material property is sufficient for LaminA/C nuclei. We then set *c*=1 and used the Matlab

303   algorithm "fmincon" optimization algorithm with a step tolerance of 1×10^{-9} to find the *b* values

304   that minimized the root mean square error for three "training" nuclei (nuclei 1, 2 and 3) for both

305   chromatin and LaminA/C groups. This step resulted in an optimized *b* value of 6.3×10^{-7} μN/μm^2

306   with an error of 5.5×10^{-5} μN/μm^2 for chromatin. For LaminA/C, the b mean value was 8.64×10^{-7}

307   μN/μm^2 with an error of 3.1×10^{-4} μN/μm^2.

308

309   <u>Linear conversion model is distinct from a homogeneous model for chromatin</u>

310   To test the differences between the homogeneous and linear-elastic heterogeneous models, the

311   homogeneous chromatin models were made from the chromatin structures of nuclei #1 - #3 by

312   setting all the elements to same elastic modulus. The modulus value was determined via

313   minimizing the RMSE between the load-displacement curves of the *in silico* and experimental

314   AFM data of the LaminA/C depleted nuclei, producing a modulus of elasticity of 2.7×10^{-4}

315     $\mu N/\mu m^2$ with a RMSE value of 6.2×10^{-5} $\mu N/\mu m^2$. There was no statistical difference between the

316   error of the homogeneous and linear-elastic heterogenous models (p=.83). Similarly, applying

317   the error-minimized *b* values to homogenous and heterogeneous models generated from the

318   test nuclei (#4 and #5) resulted in RMSE values of 6.2×10^{-5} $\mu N/\mu m^2$ and 5.5×10^{-5} $\mu N/\mu m^2$ with

319   similar error values (p=.63), suggesting that the bulk nuclei response can be modeled using

320   either homogenous or heterogeneous models (**Table 1**).

321

322   Next, the *in silico* cross-sectional Von Mises stress during the 1 µm indentation of the tip was

323   compared between the homogeneous and heterogeneous chromatin models of nuclei #4 and

324   #5. To compare the average Von Mises stresses between heterogeneous and homogeneous

325   model simulations, average Von Mises stresses at mid-sagittal planes were plotted and

326   compared across a 1 µm region of interest located between nuclear heights Z=5 µm and Z= 6

327   µm. The von mises stresses from each element within the models of each group were plotted

328   and statistically compared between the two groups.

329

330   The heterogenous models of nuclei #4 (top) and #5 (bottom) showed higher peaks at the

331   nuclear periphery of the region of interest **(Fig. 7b)**. Quantification of the peripheral peak

332   stresses showed 16% greater stresses in the heterogenous model when compared to the

333   homogenous model (p<0.001). The heterogeneous model also showed more efficient load

334   carrying as shown by lower peak stresses that were distributed among more elements when

335   compared to the homogenous model where a smaller number of elements had to carry greater

336   loads **(Fig. 7c)**.

337

Discussion

Deformation of the nucleus regulates gene transcription via altering both DNA confirmation[22] and the nuclear entry of transcription factors such as YAP/TAZ[23]. Nuclear deformation in response to mechanical forces is modulated by the mechanical stiffness provided by chromatin and LaminA/C within the nucleus[13]. The computational framework developed here was able to capture geometrical and structural inhomogeneities of both LaminA/C and chromatin from confocal images. Using constants derived from the calibration of AFM voxel-intensities to elastic moduli, mechanical behavior of nuclei were predicted merely from images without performing a physical mechanical test. The inherent limitation of this approach is that prior to predicting nuclear mechanical properties, a relatively large sample of AFM and confocal images is necessary. Further, while it was outside of the scope of the current study, errors associated with experiment-to-experiment variability of confocal images will need to be evaluated in future studies. Finally, for these predictions to be accurate, the nucleus has to be isolated from the cell as the cytoskeletal contribution to mechanical properties obtained from AFM cannot be avoided in intact cells. Even with these limitations, our method enables the prediction of nuclear stiffness and intra-nuclear deformation with only a simple nuclear isolation protocol and confocal imaging. The mechanical models of isolated, standalone nuclei developed here may also provide mechanistic insight into cellular mechanics and provide a basis for developing mechanical models of nuclei in intact cells in the future.

Our model provides a number of advantages over finite element analyses of the cell nucleus that tend to model the nucleus as a homogenous material with idealized geometry.[24,25] While comparisons between homogenous and heterogenous nuclear structures showed no significant changes in the "bulk" structural response under in silico AFM experiments, stresses throughout the nuclear structures were different where stresses concentrations were dependent upon the chromatin and LaminA/C distribution density obtained from the original images. As chromatin

364 condensation has been shown to change due to external nuclear loading[26], these models may

365 provide useful predictions of which regions of chromatin are experiencing larger loads.

366

367 Another potential advantage of this modeling system is the incorporation of nuclear envelope

368 proteins into the generated models. In this study, we modeled LaminA/C as a heterogeneous

369 material. Interestingly, the levels of LaminA/C within the nucleus have been shown to change

370 under microgravity[23]. With our model it may be possible to predict the changes in nuclear

371 stiffness due to alterations in LaminA/C levels. Further, the structural contributions of other

372 nuclear envelope proteins such as nuclear pore complexes can also be incorporated into these

373 models in the future, providing a robust computational framework for studying the forces on a

374 number of nuclear proteins.

375

376 Previous research described the nucleus's mechanical elasticity as either linear elastic or

377 hyperelastic[20]. During our experiments we chose to model the nucleus as linear elastic. As both

378 homogenous and linear conversion models of nucleus #4 and #5 produced linear force-

379 displacement curves, we also implemented hyperelastic Mooney-Rivlin and Neo-Hookean

380 material definitions[20] which again produced linear force-displacement relationships (Fig. S2),

381 suggesting that the shape of *in silico* loading curves were independent of the use of hyperelastic

382 Mooney-Rivlin and Neo-Hookean models. Corroborating these in silico findings, as shown in

383 Fig. S5, 38% of the AFM-tested nuclei showed linear loading curves.

384

385 In summary, we generated individual finite element models of nuclei from confocal images.

386 Importantly, these models were tuned to match experimental AFM results, generating a similar

387 bulk mechanical behavior when compared to a homogeneous nuclear structure. We also

388 demonstrated that if a proper relation between chromatin stiffness and image intensity is found,

389 our method can be used to model internal chromatin dynamics within the nucleus. Ultimately,

390   our study may lead to more effective techniques and insight into mechanobiological phenomena

391   within the cell nucleus, elucidating cell nucleus plasticity in response to the application of

392   mechanical forces.

393

394   **Acknowledgements**

398

399   **Table. 1:** Chromatin Material Optimization Data

	Linear conversion	Homogeneous model
B factor/elasticity	6.3 x10^{-7} µN/µm^2	2.8 x10^{-4} µN/µm^2
Average error of testing set	5.5 x10^{-5} µN/µm^2	6.2 x10^{-5} µN/µm^2

400

401   **Figure 1. siRNA mediated depletion of LaminA/C decreases isolated nuclei stiffness.** a)

402   Two groups of MSCs were grown in 10 % fetal bovine serum. One group received the LaminA/C

403   specific siRNA treatment while the other group was treated with control siRNA. Nuclei were

404   isolated and subsequently subjected to AFM testing. Nuclei of both the control group (n=30)

405   and the laminA/C knockdown group (n=73) were indented by 1 µm using a spherical tip with a

406   diameter of 6 µm. b) Confocal microscopy images of a nucleus stained for chromatin (Hoechst

407   33342) and laminA/C (cell signaling mAB4777). c) Average (± SD) force-displacement curves

408   for control nuclei (red) and laminA/C siRNA nuclei (blue). The average force-displacement curve

409   for each group is shown as a solid line; less than one standard deviation is shown as shaded

410   area. The purple area represents the overlap of the red and blue areas.

411

412   **Figure 2. Generation of image-based nucleus model.** a) Images of MSC nuclei were

413   manually segmented using Amira to isolate the nuclear geometry. b) Segmented images were

414   then used to create a surface mesh of the nucleus geometry. c) The surface image was

415   converted into a volumetric mesh. d) The volumetric mesh was assigned material properties

416   using the voxel intensity of the original image and the shown equation. e) Image of simulated

417   atomic force microscopy (AFM) experiment with the AFM tip shown in yellow, the

418   heterogeneous nucleus in blue, and the encastered base nodes in red. f) Cross sectional

419   images of the nucleus model before compression (left) and after compression (right).

420

421   **Figure 3. Element size sensitivity analysis.** a) Cross sectional images of nuclei models

422   created with elements that have an average element size of of 5, 4, 3, 2, 1, .8, and .6 μm^3.

423   Material parameters were set to b=20 kPa and c=1. Color maps indicate the corresponding

424   stiffness values. b) Graph of how maximum force, measured at the AFM tip pressing onto the

425   nucleus, versus the element size averaged for three nuclei. The solid line represents the mean

426   and the shaded area indicates the area within one standard deviation. Element sizes smaller

427   than 1 μm^3 did not affect maximum force and standard deviation (green dashed line).

428

429   **Figure 4. Element size error analysis.** Representative sagittal plane images with element

430   volumes of 3, 2, 1.5, 0.8, 0.6, and 0.3 μm^3 (2nd row) were compared against the matching

431   location in the original confocal image (3rd row). Quantification of the pixel-by-pixel intensity

432   values were represented by a % change heat map (4th row). Average % error in 3 and 0.3 μm^3

433   element volumes were 12.3% and 4.3%, respectively.

434

435   **Figure 5. Optimization of LaminA/C knockdown nuclei shows a linear elasticity**

436   **relationship.** a) Error surfaces for 3 LaminA/C depleted nuclei showed a rut-like error when

437   using different b and c values. b) Higher resolution error surfaces were generated around the

438   lowest points of the original surface. These error surfaces produced minimum values on the

439   order of 10^{-4}, similar to the error surface generated around c=1, demonstrating that there is a

440   correlation between b and c.

441

442   **Figure 6. Optimization data for control nuclei using linear and exponential conversion**

443   **factors.** a) Error surfaces for 3 control nuclei show a rut like error when using different b and c

444   values. b) Higher resolution error surfaces were then done around the lowest points of the

445   original surface, these error surfaces produces minimum values around 10^{-4} similar to the error

446   surface generated around c=1 showing that there is a correlation between b and c.

447

448   **Figure 7. Linear conversion vs homogeneous model for chromatin.** a) The simulated force

449   curves were superimposed onto the LaminA/C KO results, comparing the resulting force curves

450   from the linear conversion (left) to the results of the homogeneous model (right). b) Cross-

451   sections of the model when fully compressed were imaged (left) and the average stresses within

452   a 1 µm tall region beginning at a height of Z=5 µm were plotted (middle). Stresses within the

453   outer 25 percentile of both nuclei were plotted with a bar plot (right), showing the difference

454   between the stress distributions within the homogeneous and heterogeneous models. c) Von

455   Mises stress data was collected from the elements of both models at maximum AFM tip

456   compression and plotted within a histogram to show the difference between the stresses

457   developed within the homogeneous and heterogeneous models.

458

459   **Figure S1. Image Noise.** 5 confocal images of chromatin from nucleus 1 were separated and a

460   homogeneous section of the image was then selected from each image. This section was used

461   to quantify the image noise within the microscope by finding the average voxel intensity within

462   the images and comparing this value to the voxels within each area. The error between the

463   average voxel intensity and the accompanying area voxels was averaged to produce an

464   average error of each area. This data was averaged to produce the average noise within the

465   chromatin image of nucleus 1.

466

467   **Figure S2. Material elasticity comparison.** Nuclei simulations of nucleus 4 and 5 were

468   attempted using linear isotropic model that used the optimized values for the homogeneous

469   image conversion (left). Mooney-Rivlin models were then created by converting the

470   homogeneous optimized elasticity to Mooney-Rivlin constants as indicated within previous

471   research[15] by where c01 was set to 0 and c10 was formed by dividing the linear isotropic

472   elasticity by 6 (middle). From this point, 5 nuclei were formed by creating a Neo-Hookean

473   material model by dividing the homogeneous optimized elasticity by 6 to form the Neo Hookean

474   material constants as explained within the Abaqus user manual.

475

476   **Figure S3. Chromatin material models.** Finite element models of the nucleus have been

477   defined with the chromatin images using both the homogeneous conversion factors and the

478   heterogeneous conversion factors with a cross section of the nucleus models defined with the

479   heterogeneous model shown on the left and cross sections of the homogeneous models shown

480   on the right showing the material values using a color scale shown on the far right.

481

482   **Figure S4. Heterogeneous vs Homogeneous stress distribution.** Nuclei models 1-5 were

483   created with optimized heterogeneous and homogeneous conversion factors. The nucleus

484   models then underwent a simulated atomic force microscopy experiment with nucleus cross

485   sections for the heterogeneous nuclei showing stress dispersions dependent on the chromatin

486   density within the original images (left) as well as homogeneous models showing a stress

487   dispersion not dependent on the original chromatin density (right).

488

489   **Figure S5. Atomic Force Microscopy Curves** Atomic force microscopy experiment data for

490   laminA/C knockdown nuclei (n=72, left) and control nuclei (n=30, right) has been plotted using

491   Matlab.

492

493

494   **References**

495

496   1   Pagnotti, G. M. *et al.* Combating osteoporosis and obesity with exercise: leveraging cell

497   mechanosensitivity. *Nature Reviews Endocrinology*, doi:10.1038/s41574-019-0170-1

498   (2019).

499   2   Engler, A. J., Sen, S., Sweeney, H. L. & Discher, D. E. Matrix elasticity directs stem cell

500   lineage specification. *Cell* **126**, 677-689, doi:10.1016/j.cell.2006.06.044 (2006).

501   3   Hanna, H., Mir, L. M. & Andre, F. M. In vitro osteoblastic differentiation of mesenchymal

502   stem cells generates cell layers with distinct properties. *Stem Cell Res Ther* **9**, 203,

503   doi:10.1186/s13287-018-0942-x (2018).

504   4   Humphrey, J. D., Dufresne, E. R. & Schwartz, M. A. Mechanotransduction and

505   extracellular matrix homeostasis. *Nature reviews. Molecular cell biology* **15**, 802-812,

506   doi:10.1038/nrm3896 (2014).

507   5   Andalib, M. N., Lee, J. S., Ha, L., Dzenis, Y. & Lim, J. Y. Focal adhesion kinase

508   regulation in stem cell alignment and spreading on nanofibers. *Biochemical and*

509   *biophysical research communications* **473**, 920-925, doi:10.1016/j.bbrc.2016.03.151

510   (2016).

511 6 Harris, A. R., Jreij, P. & Fletcher, D. A. Mechanotransduction by the Actin Cytoskeleton:

512   Converting Mechanical Stimuli into Biochemical Signals. *Annual Review of Biophysics*

513   **47**, 617-631, doi:10.1146/annurev-biophys-070816-033547 (2016).

514 7 Hoffman, L. M. *et al.* Mechanical stress triggers nuclear remodeling and the formation of

515   Transmembrane Actin Nuclear lines with associated Nuclear Pore Complexes.

516   *Molecular biology of the cell*, mbc.E19-01-0027, doi:10.1091/mbc.E19-01-0027 (2020).

517 8 Shiu, J.-Y., Aires, L., Lin, Z. & Vogel, V. Nanopillar force measurements reveal actin-

518   cap-mediated YAP mechanotransduction. *Nature cell biology* **20**, 262-271,

519   doi:10.1038/s41556-017-0030-y (2018).

520 9 Le, H. Q. *et al.* Mechanical regulation of transcription controls Polycomb-mediated gene

521   silencing during lineage commitment. *Nature cell biology* **18**, 864-875,

522   doi:10.1038/ncb3387 (2016).

523 10 Makhija, E., Jokhun, D. S. & Shivashankar, G. V. Nuclear deformability and telomere

524   dynamics are regulated by cell geometric constraints. *Proceedings of the National*

525   *Academy of Sciences of the United States of America* **113**, E32-40,

526   doi:10.1073/pnas.1513189113 (2016).

527 11 Darling, E. M. & Di Carlo, D. High-Throughput Assessment of Cellular Mechanical

528   Properties. *Annual review of biomedical engineering* **17**, 35-62, doi:10.1146/annurev-

529   bioeng-071114-040545 (2015).

530 12 Ghosh, S. *et al.* Deformation Microscopy for Dynamic Intracellular and Intranuclear

531   Mapping of Mechanics with High Spatiotemporal Resolution. *Cell reports* **27**, 1607-

532   1620.e1604, doi:10.1016/j.celrep.2019.04.009 (2019).

533 13 Martins, R. P., Finan, J. D., Farshid, G. & Lee, D. A. Mechanical Regulation of Nuclear

534   Structure and Function. *Annual review of biomedical engineering* **14**, 431-455,

535   doi:10.1146/annurev-bioeng-071910-124638 (2012).

536   14   Lammerding, J. *et al.* Lamins A and C but Not Lamin B1 Regulate Nuclear Mechanics.

537   *Journal of Biological Chemistry* **281**, 25768-25780, doi:10.1074/jbc.M513511200 (2006).

538   15   Stephens, A. D., Banigan, E. J. & Marko, J. F. Separate roles for chromatin and lamins

539   in nuclear mechanics. *Nucleus (Austin, Tex.)* **9**, 119-124,

540   doi:10.1080/19491034.2017.1414118 (2018).

541   16   Stephens, A. D. *et al.* Chromatin histone modifications and rigidity affect nuclear

542   morphology independent of lamins. *Molecular biology of the cell* **29**, 220-233,

543   doi:10.1091/mbc.E17-06-0410 (2018).

544   17   Peister, A. *et al.* Adult stem cells from bone marrow (MSCs) isolated from different

545   strains of inbred mice vary in surface epitopes, rates of proliferation, and differentiation

546   potential. *Blood* **103**, 1662-1668, doi:10.1182/blood-2003-09-3070 (2004).

547   18   Bas, G. *et al.* Low Intensity Vibrations Augment Mesenchymal Stem Cell Proliferation

548   and Differentiation Capacity during in vitro Expansion. *Scientific reports* **10**, 9369,

549   doi:10.1038/s41598-020-66055-0 (2020).

550   19   Sankaran, J. S. *et al.* Knockdown of formin mDia2 alters lamin B1 levels and increases

551   osteogenesis in stem cells. *Stem Cells* **38**, 102-117, doi:10.1002/stem.3098 (2020).

552   20   Tang, G., Galluzzi, M., Zhang, B., Shen, Y. L. & Stadler, F. J. Biomechanical

553   Heterogeneity of Living Cells: Comparison between Atomic Force Microscopy and Finite

554   Element Simulation. *Langmuir : the ACS journal of surfaces and colloids* **35**, 7578-7587,

555   doi:10.1021/acs.langmuir.8b02211 (2019).

556   21   Newberg, J. *et al.* Isolated Nuclei Stiffen in Response to Low Intensity Vibration. *Journal*

557   *of biomechanics*, 110012, doi:https://doi.org/10.1016/j.jbiomech.2020.110012 (2020).

558   22   Rubin, J., Styner, M. & Uzer, G. Physical Signals May Affect Mesenchymal Stem Cell

559   Differentiation via Epigenetic Controls. *Exercise and sport sciences reviews* **46**, 42-47,

560   doi:10.1249/jes.0000000000000129 (2018).

561   23   Dupont, S. *et al.* Role of YAP/TAZ in mechanotransduction. *Nature* **474**, 179-183,

562   doi:http://www.nature.com/nature/journal/v474/n7350/abs/10.1038-nature10137-

563   unlocked.html#supplementary-information (2011).

564   24   Wang, L., Wang, L., Xu, L. & Chen, W. Finite Element Modelling of Single Cell Based on

565   Atomic Force Microscope Indentation Method. *Computational and Mathematical*

566   *Methods in Medicine* **2019**, 7895061, doi:10.1155/2019/7895061 (2019).

567   25   McGarry, J. G. & Prendergast, P. J. A three-dimensional finite element model of an

568   adherent eukaryotic cell. *European cells & materials* **7**, 27-33; discussion 33-24 (2004).

569   26   Heo, S. J. *et al.* Biophysical Regulation of Chromatin Architecture Instills a Mechanical

570   Memory in Mesenchymal Stem Cells. *Scientific reports* **5**, 16895, doi:10.1038/srep16895

571   (2015).

572

573

Figure 1
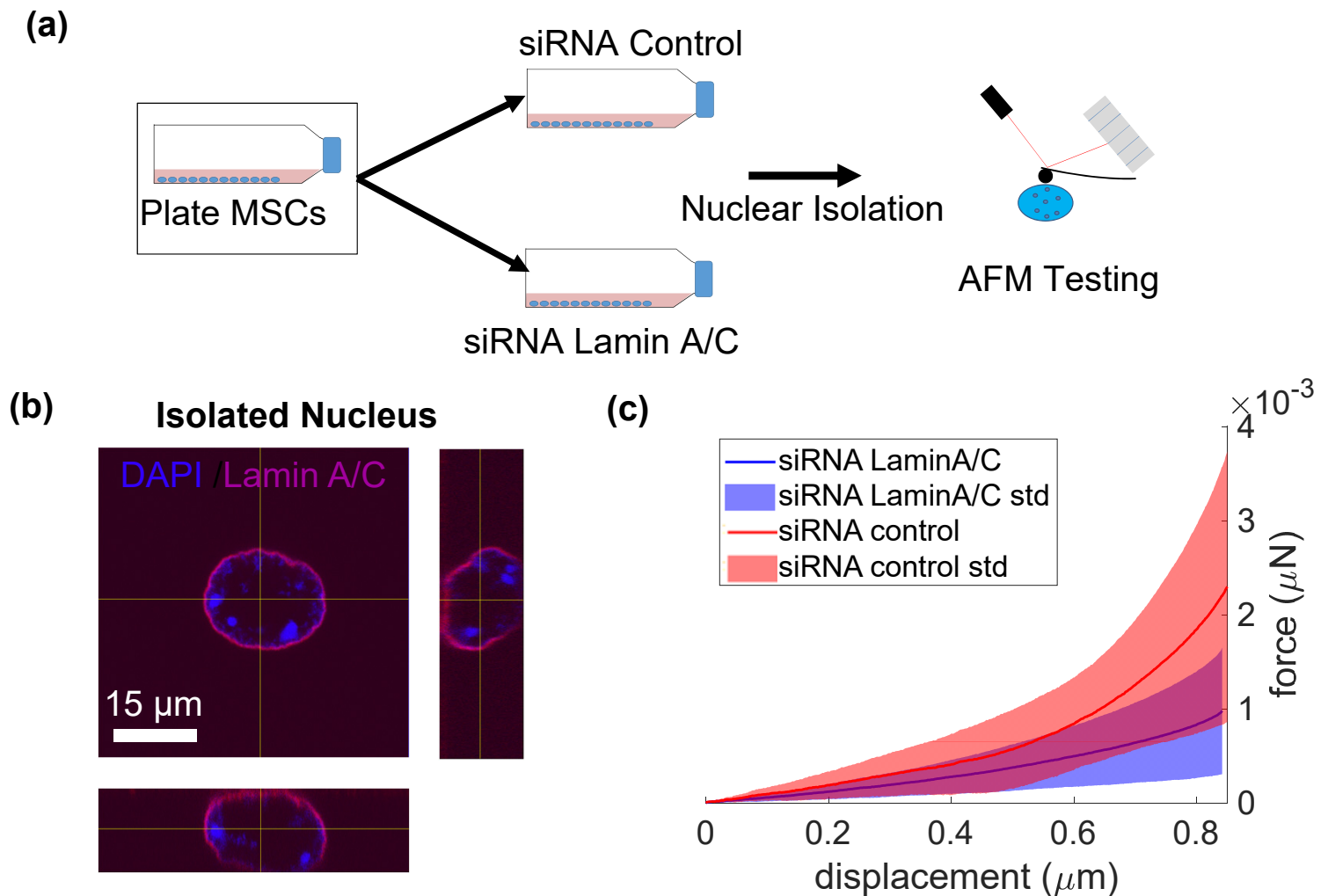
Figure 1. siRNA mediated depletion of LaminA/C decreases isolated nuclei stiffness. a) Two groups of MSCs were grown in 10 % fetal bovine serum. One group received the LaminA/C specific siRNA treatment while the other group was treated with control siRNA. Nuclei were isolated and subsequently subjected to AFM testing. Nuclei of both the control group (n=30) and the laminA/C knockdown group (n=73) were indented by 1 μm using a spherical tip with a diameter of 6 μm. b) Confocal microscopy images of a nucleus stained for chromatin (Hoechst 33342) and laminA/C (cell signaling mAB4777). c) Average (± SD) force-displacement curves for control nuclei (red) and laminA/C siRNA nuclei (blue). The average force-displacement curve for each group is shown as a solid line; less than one standard deviation is shown as shaded area. The purple area represents the overlap of the red and blue areas.

Figure 2

(a) Segmentation   **(b) Surface mesh**   **(c) Volume mesh**

(d) Assign intensity based on material property

$$E = a + b * HU^c$$

(e) Set up simulation   **(f) Run simulation**
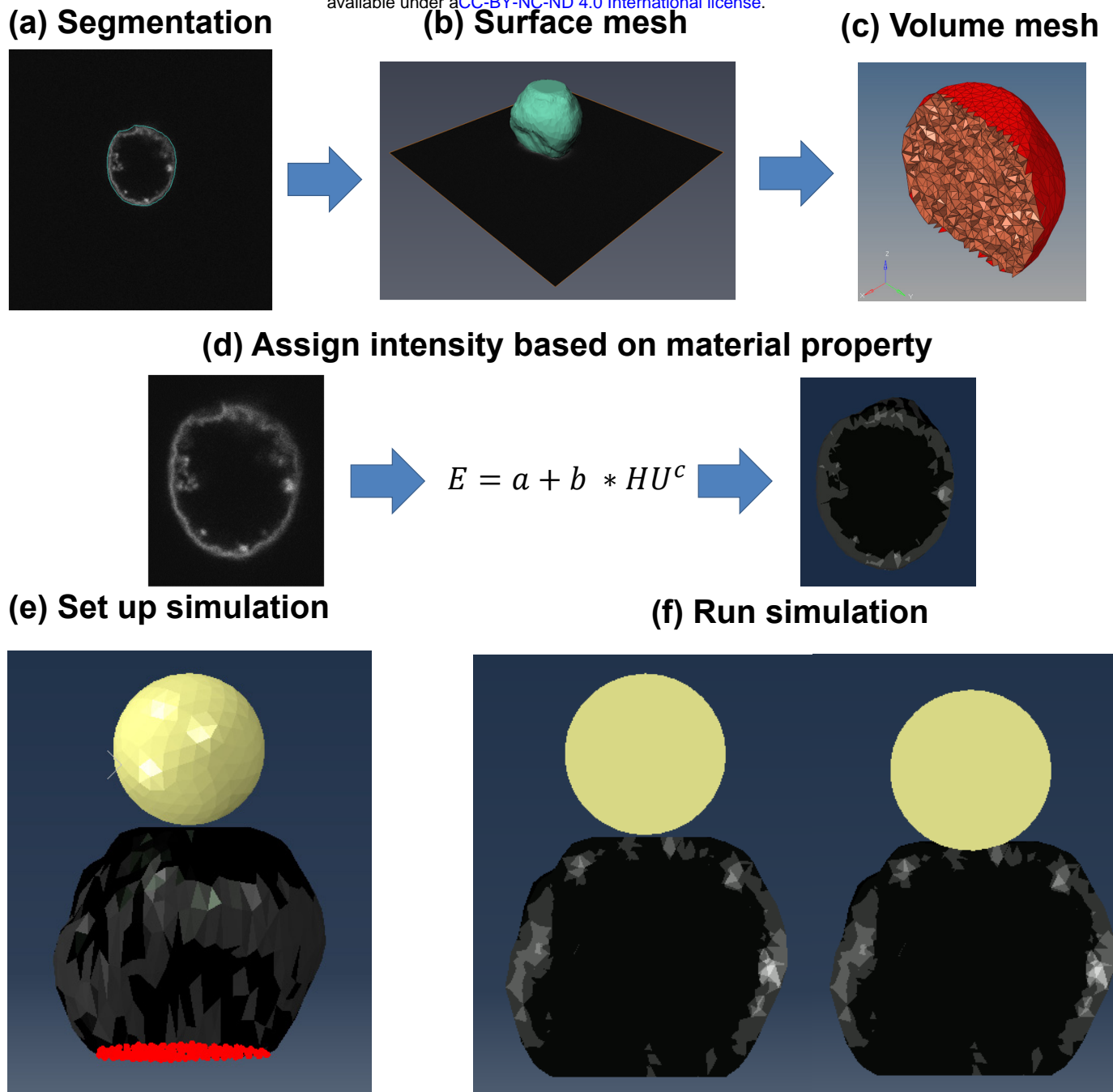
Figure 2. Generation of image-based nucleus model. a) Images of MSC nuclei were manually segmented using Amira to isolate the nuclear geometry. b) Segmented images were then used to create a surface mesh of the nucleus geometry. c) The surface image was converted into a volumetric mesh. d) The volumetric mesh was assigned material properties using the voxel intensity of the original image and the shown equation. e) Image of simulated atomic force microscopy (AFM) experiment with the AFM tip shown in yellow, the heterogeneous nucleus in blue, and the encastered base nodes in red. f) Cross sectional images of the nucleus model before compression (left) and after compression (right).
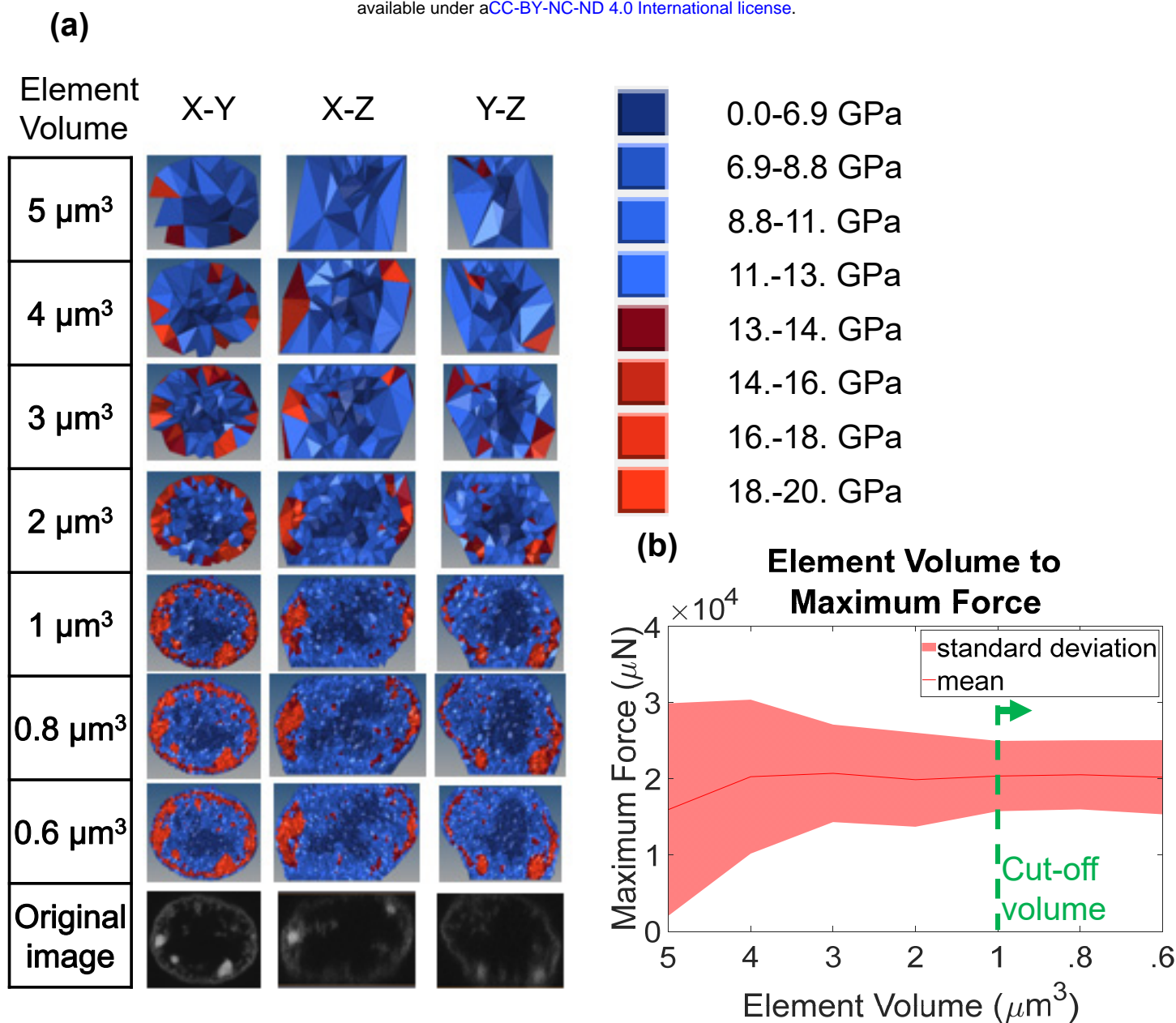
Figure 3

Figure 3. Element size sensitivity analysis. a) Cross sectional images of nuclei models created with elements that have an average element size of of 5, 4, 3, 2 ,1, .8, and .6 μm^3. Material parameters were set to b=20 kPa and c=1. Color maps indicate the corresponding stiffness values. b) Graph of how maximum force, measured at the AFM tip pressing onto the nucleus, versus the element size averaged for three nuclei. The solid line represents the mean and the shaded area indicates the area within one standard deviation. Element sizes smaller than 1 μm^3 did not affect maximum force and standard deviation (green dashed line).

Figure 4

Element Volume	3 µm³	2 µm³	1.5 µm³	1 µm³	.8 µm³	.6 µm³	.3 µm³
Mesh Image							
Original Image							
% Error							
Average % Error	12.3%	9.2%	7.9%	6.4%	5.8%	5%	4.3%

0 %   150 %
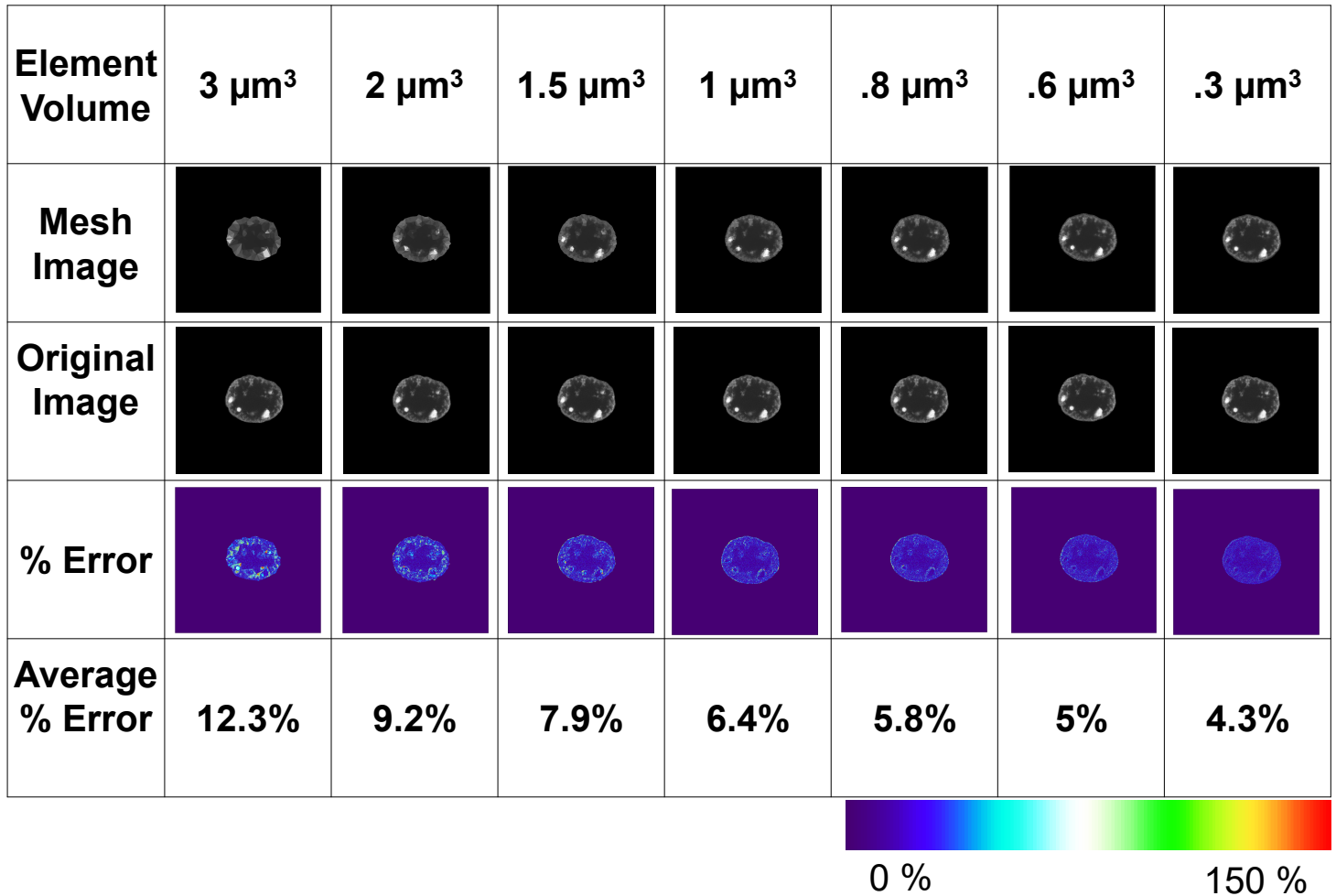
Figure 4. Element size error analysis. Representative sagittal plane images with element volumes of 3, 2, 1.5, 0.8, 0.6, and 0.3 µm³ (2nd row) were compared against the matching location in the original confocal image (3rd row). Quantification of the pixel-by-pixel intensity values were represented by a % change heat map (4th row). Average % error in 3 and 0.3 µm³ element volumes were 12.3% and 4.3%, respectively.

Figure 5
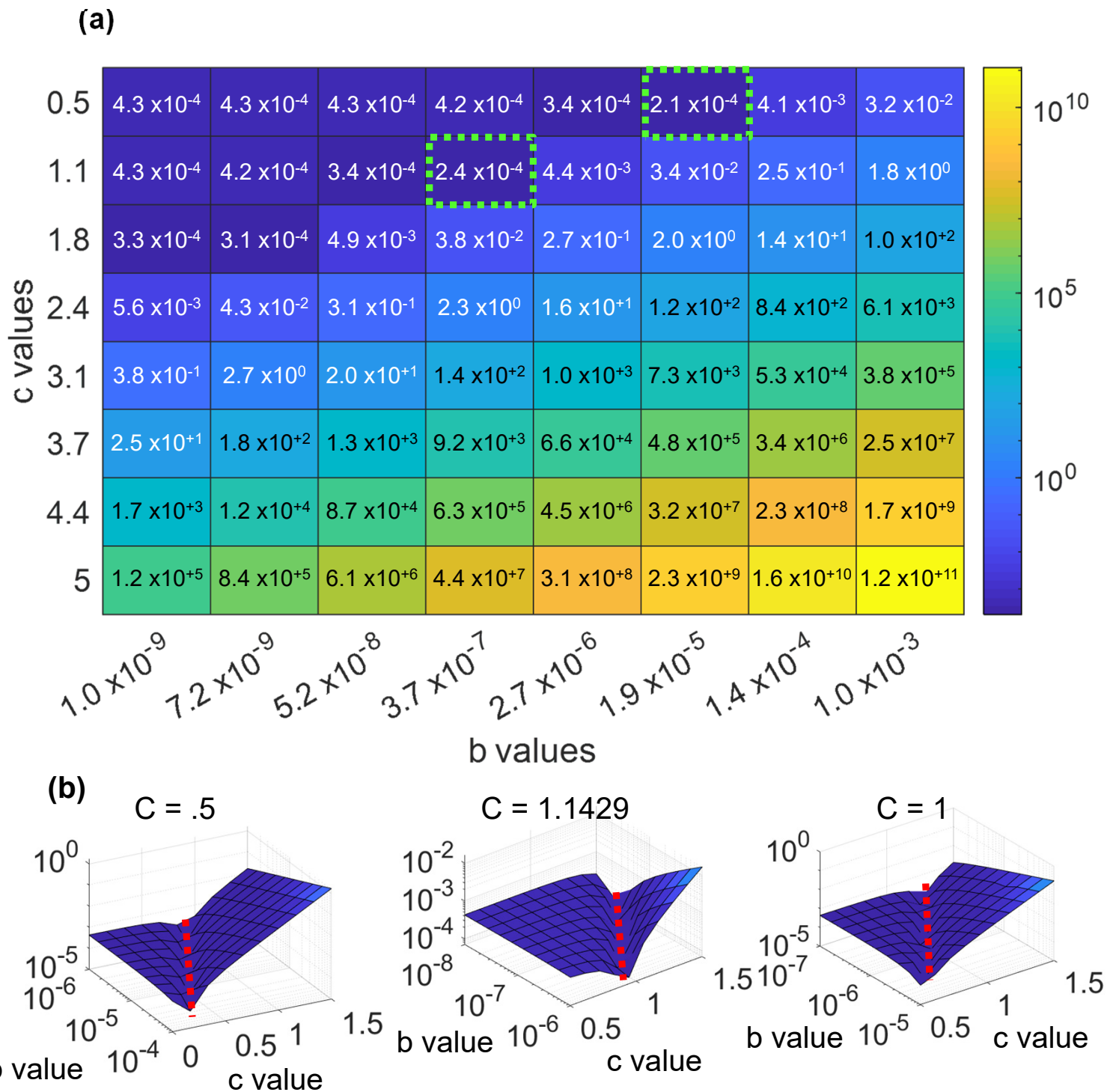
Figure 5. Optimization of LaminA/C knockdown nuclei shows a linear elasticity relationship. a) Error surfaces for 3 LaminA/C depleted nuclei showed a rut-like error when using different b and c values. b) Higher resolution error surfaces were generated around the lowest points of the original surface. These error surfaces produced minimum values on the order of 10^{-4}, similar to the error surface generated around c=1, demonstrating that there is a correlation between b and c.
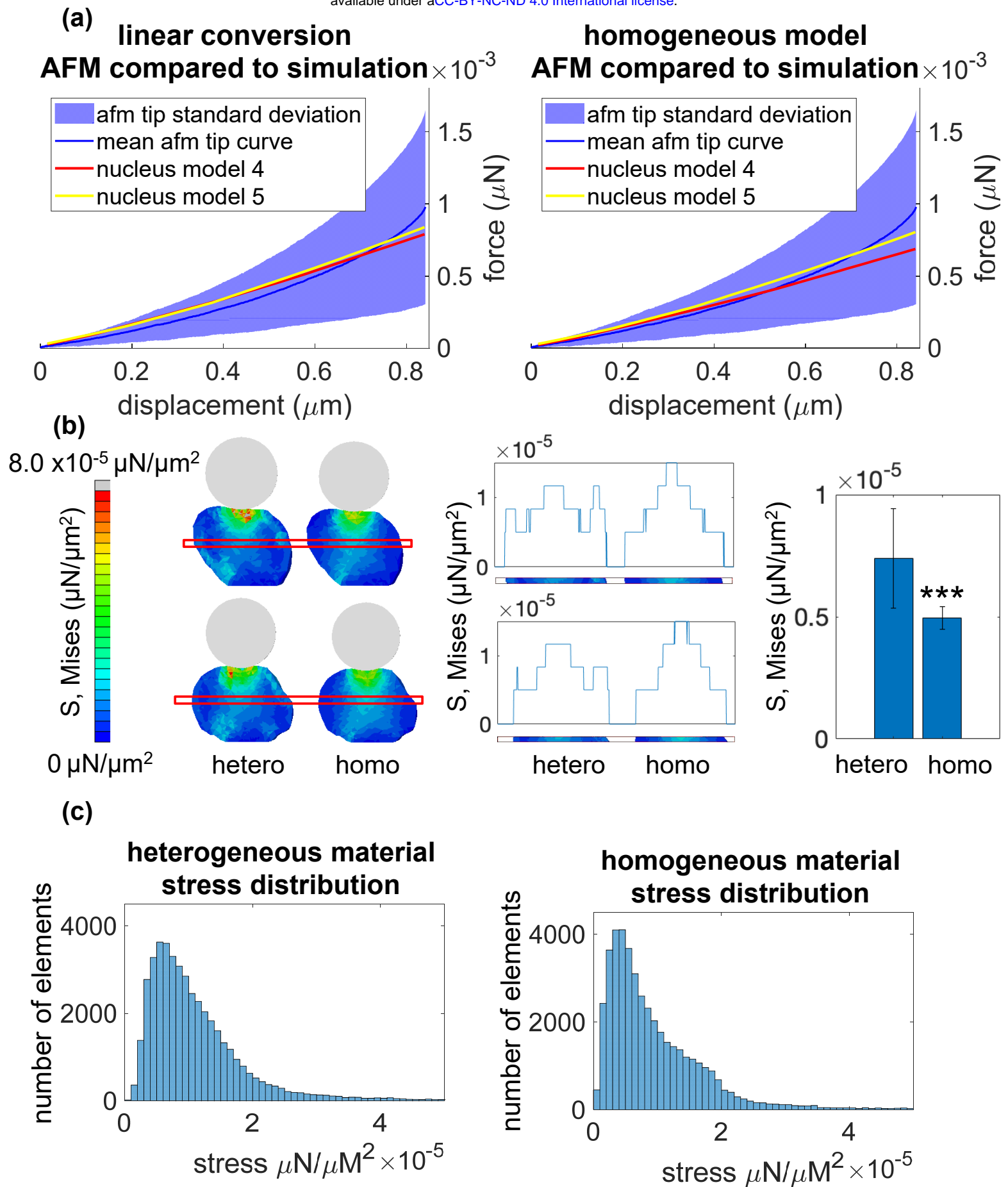
Figure 6
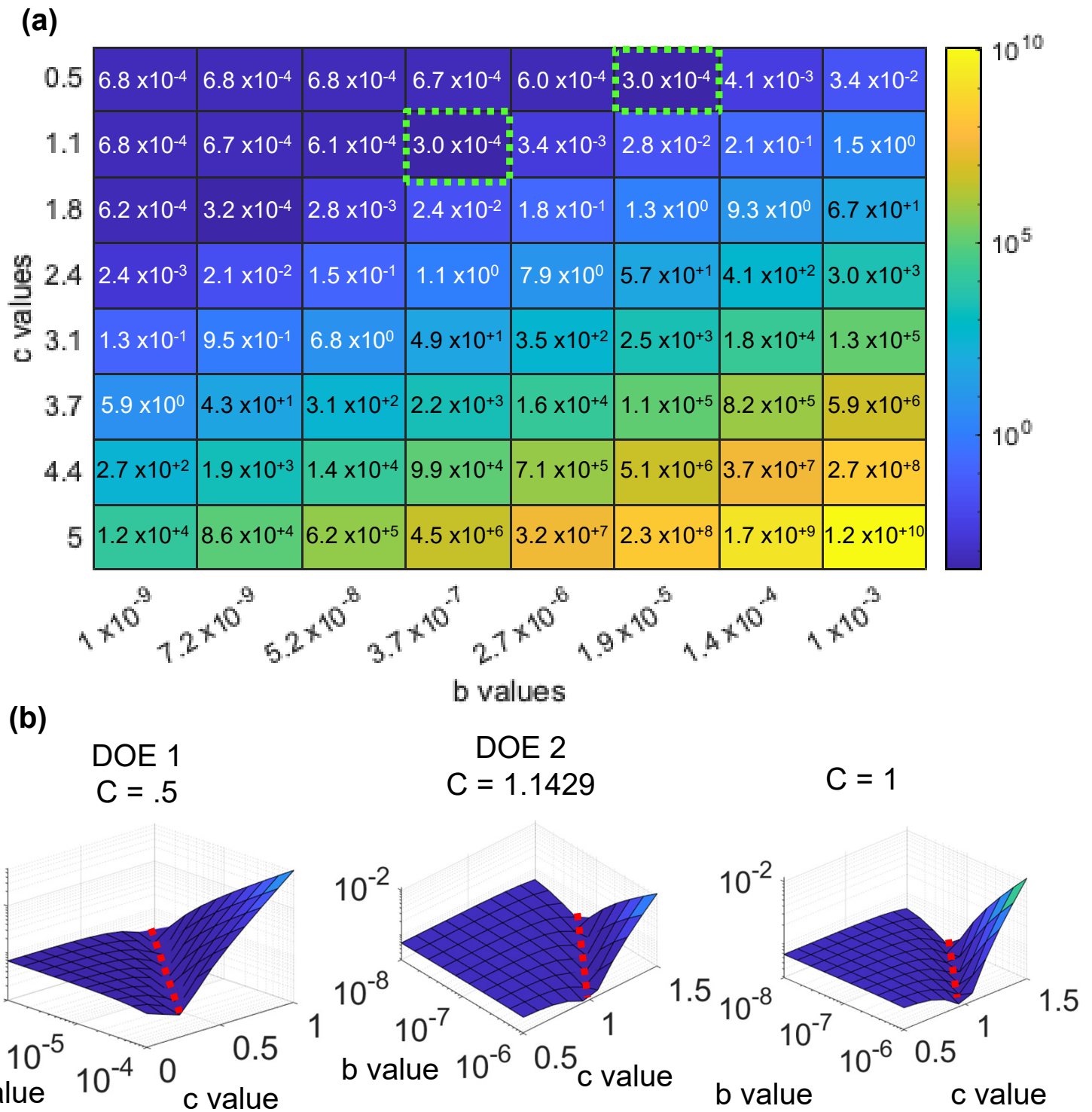
Figure 6. Optimization data for control nuclei knockdown using linear and exponential conversion factors. a) Error surfaces for 3 control nuclei showed a rut like error when using different b and c values. b) Higher resolution error surfaces were generated around the lowest points of the original surface. These error surfaces produced minimum values on the order of 10^{-4}, similar to the error surface generated around c=1, demonstrating that there is a correlation between b and c.

Figure 7

(a)

linear conversion AFM compared to simulation

homogeneous model AFM compared to simulation

(b)

(c)

heterogeneous material stress distribution

homogeneous material stress distribution

Figure 7. Linear conversion vs homogeneous model for chromatin. a) The simulated force curves were superimposed onto the LaminA/C KO results, comparing the resulting force curves from the linear conversion (left) to the results of the homogeneous model (right). b) Cross-sections of the model when fully compressed were imaged (left) and the average stresses within a 1 µm tall region beginning at a height of Z=5 µm were plotted (middle). Stresses within the outer 25 percentile of both nuclei were plotted with a bar plot (right), showing the difference between the stress distributions within the homogeneous and heterogeneous models. c) Von Mises stress data was collected from the elements of both models at maximum AFM tip compression and plotted within a histogram to show the difference between the stresses developed within the homogeneous and heterogeneous models.

Supplementary Information

Modeling stem cell nucleus mechanics using confocal microscopy

Kennedy Z[1], Newberg J[1], Goelzer M[1], Stefan Judex[2], Fitzpatrick CK[1], Uzer G[1] [†]

[1]Mechanical and Biomedical Engineering, Boise State University
[2]Biomedical Engineering, Stony Brook University

† Corresponding Author

Supplementary Figure 1
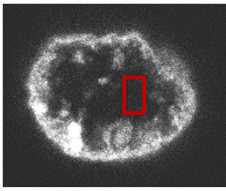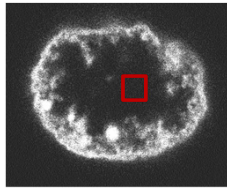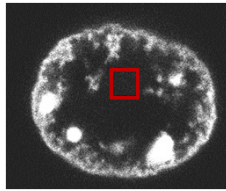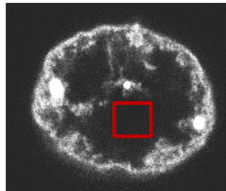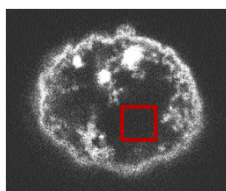
Image noise data					
	1st area	2nd area	3rd area	4th area	5th area
Image of area selected					
Area average error	14.%	13.%	13.%	12.%	13%
Total average error	13.%				

Figure S1. Image Noise. 5 confocal images of chromatin from nucleus 1 were separated and a homogeneous section of the image was then selected from each image. This section was used to quantify the image noise within the microscope by finding the average voxel intensity within the images and comparing this value to the voxels within each area. The error between the average voxel intensity and the accompanying area voxels was averaged to produce an average error of each area. This data was averaged to produce the average noise within the chromatin image of nucleus 1.
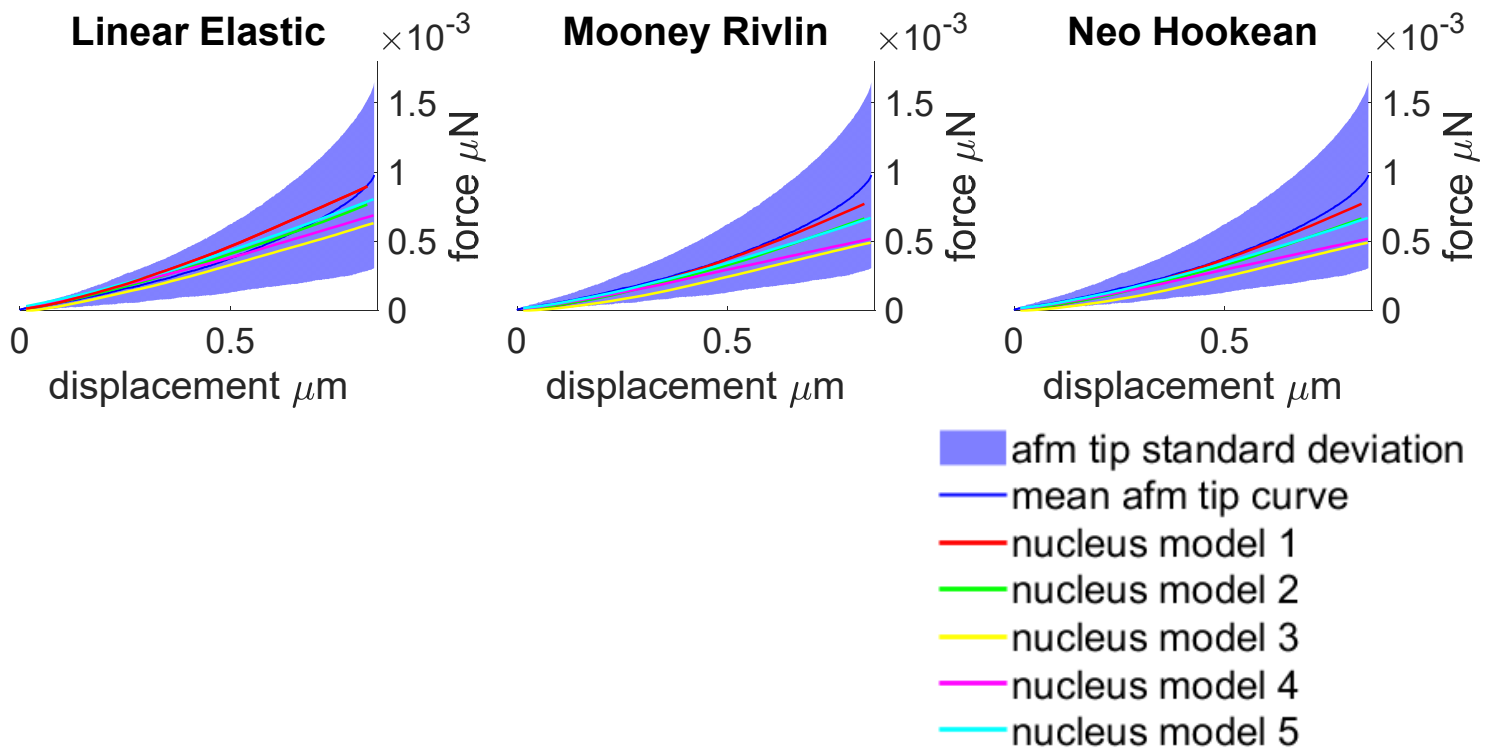
Figure S2. material elasticity comparison. Nuclei simulations of nucleus 4 and 5 were attempted using linear isotropic model that used the optimized values for the homogeneous image conversion(left). Mooney-Rivlin models were then created by converting the homogeneous optimized elasticity to Mooney-Rivlin constants as indicated within previous research[15] by where c01 was set to 0 and c10 was formed by dividing the linear isotropic elasticity by 6(middle). From this point, 5 nuclei were formed by creating a Neo-Hookean material model by dividing the homogeneous optimized elasticity by 6 to form the Neo Hookean material constants as explained within the Abaqus user manual.
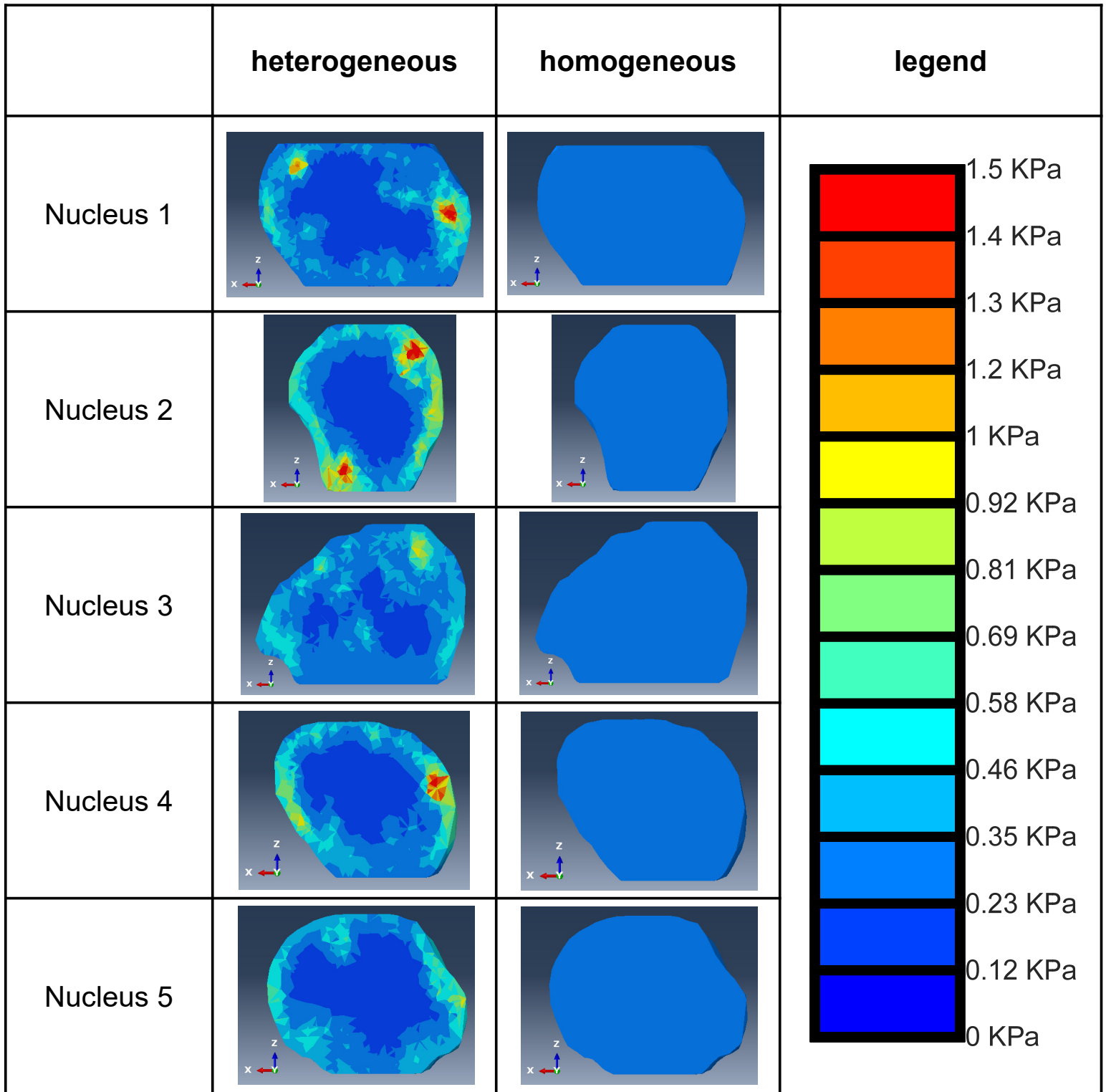
Figure S3. Chromatin material models Finite element models of the nucleus have been defined with the chromatin images using both the homogeneous conversion factors and the heterogeneous conversion factors with a cross section of the nucleus models defined with the heterogeneous model shown on the left and cross sections of the homogeneous models shown on the right showing the material values using a color scale shown on the far right.
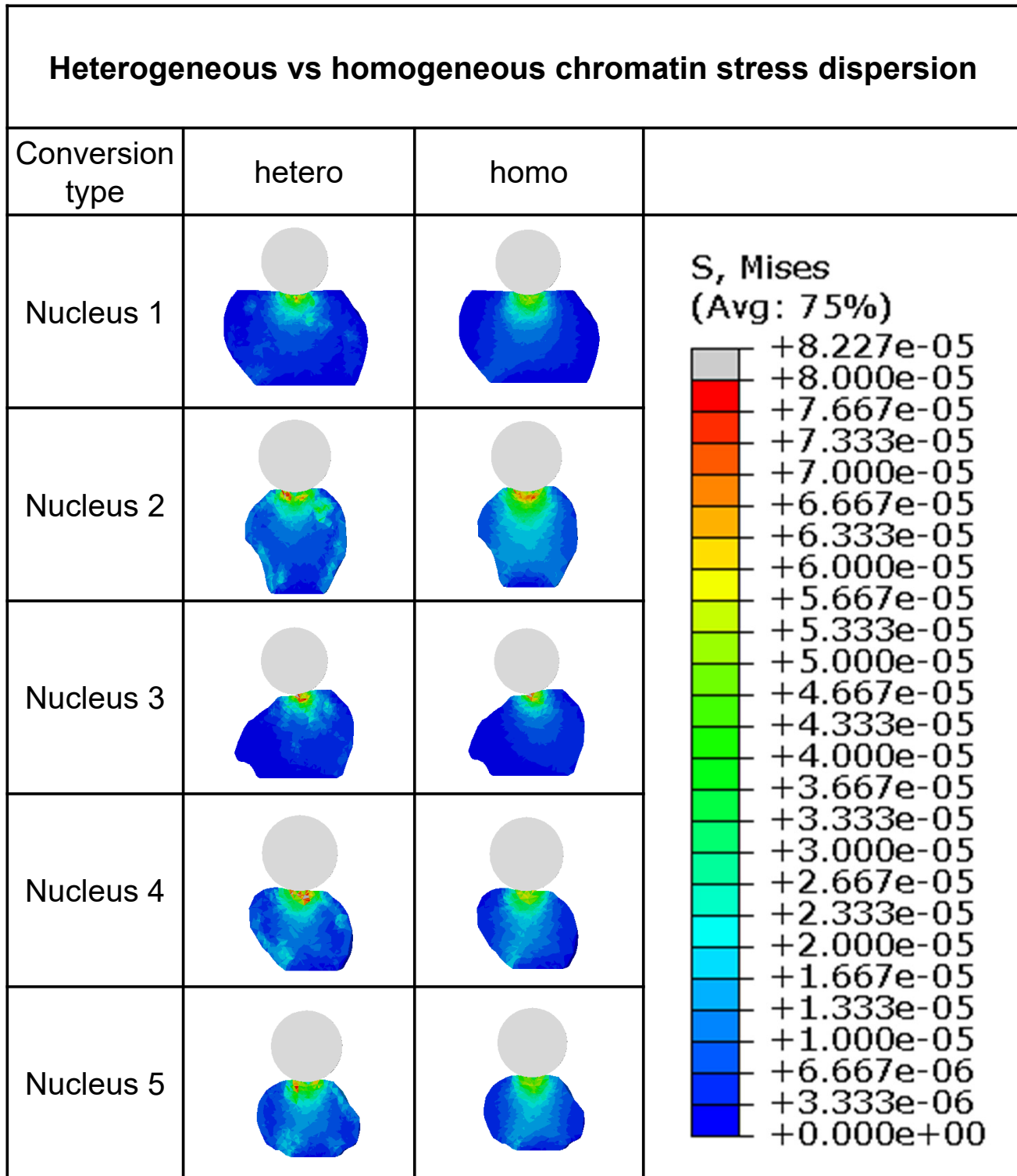
Figure S4. Heterogeneous vs Homogeneous stress distribution. Nuclei models 1-5 were created with optimized heterogeneous and homogeneous conversion factors. The nucleus models then underwent a simulated atomic force microscopy experiment with nucleus cross sections for the heterogeneous nuclei showing stress dispersions dependent on the chromatin density within the original images (left) as well as homogeneous models showing a stress dispersion not dependent on the original chromatin density (right).
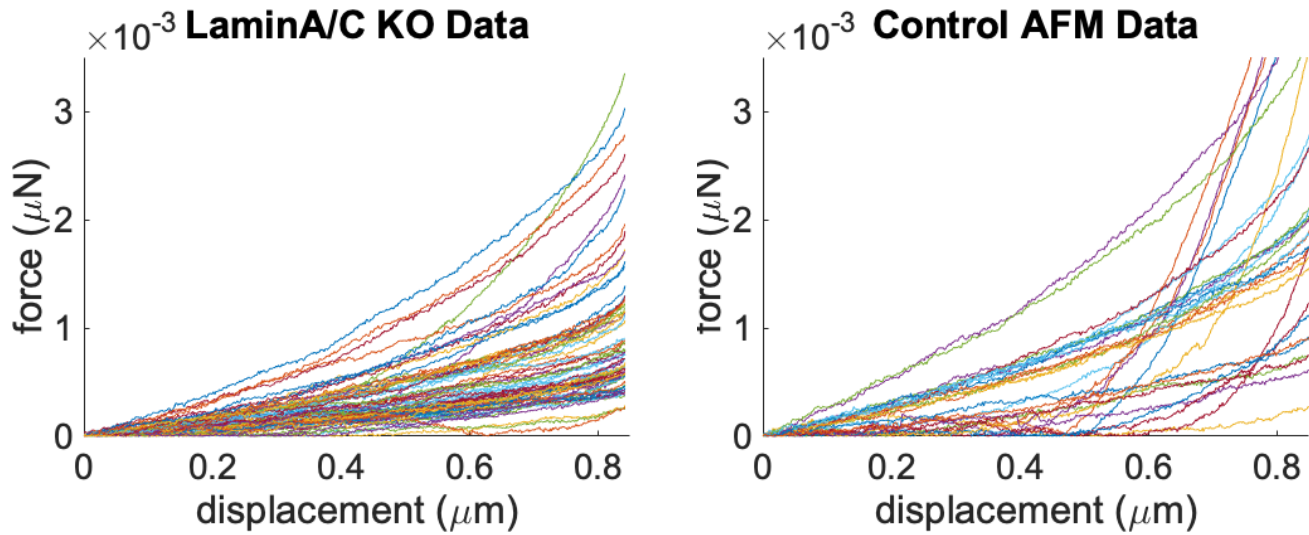
Figure S5. Atomic Force Microscopy Curves Atomic force microscopy experiment data for LaminA/C knockdown nuclei (n=72, left) and control nuclei (n=30, right) has been plotted using Matlab.